RESEARCH ARTICLE

Key Points:
- Thermally excited emissions maximize in the cusp around magnetic noon
- Peak occurrence at electron temperatures exceeding 3000 K
- Peak occurrence at electron densities exceeding 5×10^{11} m^{-3} for lower electron temperatures (2300–3000 K)

Correspondence to:
N. K. Kwagala,
norah.kwagala@uib.no

How Often Do Thermally Excited 630.0 nm Emissions Occur in the Polar Ionosphere?

Norah Kaggwa Kwagala[1,2] (ID) **, Kjellmar Oksavik[1,2,3]** (ID) **, Dag A. Lorentzen[2]** (ID) **, and Magnar G. Johnsen[4]**

[1]Birkeland Centre for Space Science, University of Bergen, Bergen, Norway, [2]Birkeland Centre for Space Science, University Centre in Svalbard, Longyearbyen, Norway, [3]Now at Center for Space Science and Engineering Research (Space@VT), Virginia Polytechnic Institute and State University, Blacksburg, VA, USA, [4]Tromsø Geophysical Observatory, UiT-Arctic University of Norway, Tromso, Norway

Abstract This paper studies thermally excited emissions in the polar ionosphere derived from European Incoherent Scatter Svalbard radar measurements from the years 2000–2015. The peak occurrence is found around magnetic noon, where the radar observations show cusp-like characteristics. The ionospheric, interplanetary magnetic field and solar wind conditions favor dayside magnetic reconnection as the dominant driving process. The thermal emissions occur 10 times more frequently on the dayside than on the nightside, with an average intensity of 1–5 kR. For typical electron densities in the polar ionosphere (2×10^{11} m^{-3}), we find the peak occurrence rate to occur for extreme electron temperatures (>3000 K), which is consistent with assumptions in literature. However, for extreme electron densities (> 5×10^{11} m^{-3}), we can now report on a completely new population of thermal emissions that may occur at much lower electron temperatures (~2300 K). The empirical atmospheric model (NRLMSISE-00) suggests that the latter population is associated with enhanced neutral atomic oxygen densities.

1. Introduction

The 630.0 and 557.7 nm lines are common emissions in the polar ionosphere, both arising from the excited states of atomic oxygen ^{1}D and ^{1}S, respectively. The lower energy ^{1}D state makes the 630.0 nm a possible emission from low-energy processes like thermal excitation. Thermal excitation of atomic oxygen in the polar ionosphere can sometimes lead to noticeable 630.0 nm emission intensities (i.e, exceeding 1 kR). This happens when the ambient electron gas is heated. If there are enough electrons in the high-energy tail of the energy distribution exceeding 1.96 eV, then the electron gas may cool by exciting atomic oxygen to the ^{1}D state, which then emits 630.0 nm photons on deexcitation. In the polar ionosphere the soft precipitating electrons are believed to be the heating source of the ambient electron gas. More detailed explanations of the theory of thermal excitation can be found in literature (e.g., Carlson et al., 2013; Kozyra et al., 1990; Kwagala et al., 2017; Lockwood, Carlson, & Sandholt, 1993; Wickwar & Kofman, 1984).

Thermally excited 630.0 nm emissions in the cusp have been reported in a number of case studies (e.g., Carlson et al., 2013; Johnsen et al., 2012; Kwagala et al., 2017; Wickwar & Kofman, 1984). To our knowledge, no studies have investigated thermally excited emissions outside the cusp region or in a statistical sense. The aim of our study is therefore to obtain a broader understanding of the overall role of thermally excited emissions in the polar ionosphere.

Our study sets out to statistically analyze the occurrence of thermal emissions in the polar ionosphere based on data from the European Incoherent Scatter (EISCAT) Svalbard Radar for the years of 2000 to 2015. Our objective is to identify when and where thermal emissions are potentially important for analyses, interpretations, and modeling of auroral emissions in the polar ionosphere.

Our approach is described in section 2, and our observations are presented in section 3. Our discussion and conclusions are found in sections 4 and 5.

2. Approach

This study is based on ionospheric measurements of electron temperature and electron density by the EISCAT Svalbard Radar (ESR) during the years from 2000 to 2015. ESR is located at 445 m altitude, 75.12°N magnetic latitude, and magnetic local time is UT + 3 (geographic coordinates: 78.15°N, 16.02°E). In order to get an

Table 1

An Overview of Time and Altitude Resolutions for the EISCAT Experiments Used in This Study

			Raw data		Processed data	
Year	Experiment name	Altitude coverage	Time resolution	Altitude resolution	Time resolution	Altitude resolution
		(km)	(s)	(km)	(s)	(km)
2000–2003	tau0	53–1144	6.4	3.0	64–128	3–37
2004–2006	steffe	34–800	6.0	2.2	60–120	3.7–30
2007–2015	ipy	28–383	6.0	2.2	60–120	3.7–30
		388–509		4.5		

unbiased database, we only use experiments for which the radar ran continuously for approximately 24 h. Measurements from the fixed magnetic field-aligned 42 m parabolic dish are used. ESR has a number of standard experiments through which measurements can be made. An overview of typical experiments in our database is shown in the Table 1. A postintegration time of 1–2 min was used for the postanalysis. The raw data consist of lag profiles that have been preintegrated for a few seconds. The processed data are postintegrated data for longer periods (e.g., 1–2 min) using the Grand Unified Incoherent Scatter Design and Analysis Package (GUISDAP) (Lehtinen & Huuskonen, 1996).

The Naval Research Laboratory Mass Spectrometer and Incoherent Scatter Radar 2000 model (NRLMSISE-00) (Picone et al., 2002) was used to generate the number density of atomic oxygen. We obtained the solar wind and interplanetary field (IMF) parameters from the GSFC/SPDF OMNI database. This data is already time shifted to the magnetopause. The GSM coordinates and 1 h averages were used. The solar wind dynamic pressure (P) is given by $P = M \times N_p \times V_p^2$, where M is the proton mass, N_p is the solar wind density, and V_p is the solar wind speed. All data used in the present study was obtained through the Madrigal database which is composed of upper atmospheric scientific data.

Mantas and Carlson (1991) reassessed different values of cross sections provided in literature (e.g., Doering and Gulcicek, 1989; Henry et al., 1969; Lan et al., 1972; Thomas and Nesbet, 1975). An earlier excitation rate, based on the cross section by Henry et al. (1969), was derived by Link (1982) and was used in some studies (e.g., Solomon et al., 1988). Mantas and Carlson (1991) found that the rates derived from the cross section by Henry et al. (1969) and Lan et al. (1972) were almost identical for practical purposes, but the cross section by Lan et al. (1972) appeared more complete based on theoretical grounds and was therefore recommended. Based on these recommendations, Carlson et al. (2013) provided a set of formulae that can be applied to incoherent scatter radar measurements to calculate and separate thermally excited 630.0 nm emissions from the total 630.0 nm emissions.

In the current study, a numerical model employing the formulae provided by Carlson et al. (2013) is used to derive the thermally excited emission rates and total intensity. For electron density N_e, electron temperature T_e, and atomic oxygen density N_o, the volume emission rate is given by

$$I_{630}(h) = \alpha \left[T_e(h) \right] \times N_o(h) \times N_e(h) \quad \text{(Rayleighs/km)} \tag{1}$$

where

$$\alpha(T_e) = 0.15 \times \sqrt{T_e} \times \frac{(8537 + T_e)}{(34191 + T_e)^3} \times e^{\left(\frac{-22756}{T_e} \right)} \quad (\text{cm}^3/\text{s}) \tag{2}$$

and the total vertical column intensity is found by integrating the volume emission rate along the line of sight

$$I_{630} = \int_{250\text{km}}^{650\text{km}} I_{630}(h) \, dh \quad \text{(Rayleighs)} \tag{3}$$

Mantas and Carlson (1991) provided equation (2) based on cross section by Lan et al. (1972), whereas Carlson et al. (2013) provided equations (1) and (3). All the parameters, N_e, T_e, and N_o are functions of the altitude h in kilometers. N_e and N_o are measured in cm^{-3} and T_e in Kelvin.

After generating the emission rates for the whole data set, we analyze the intensities for occurrence rate and probability. First, we categorize our data into two categories: strong and weak thermal components.
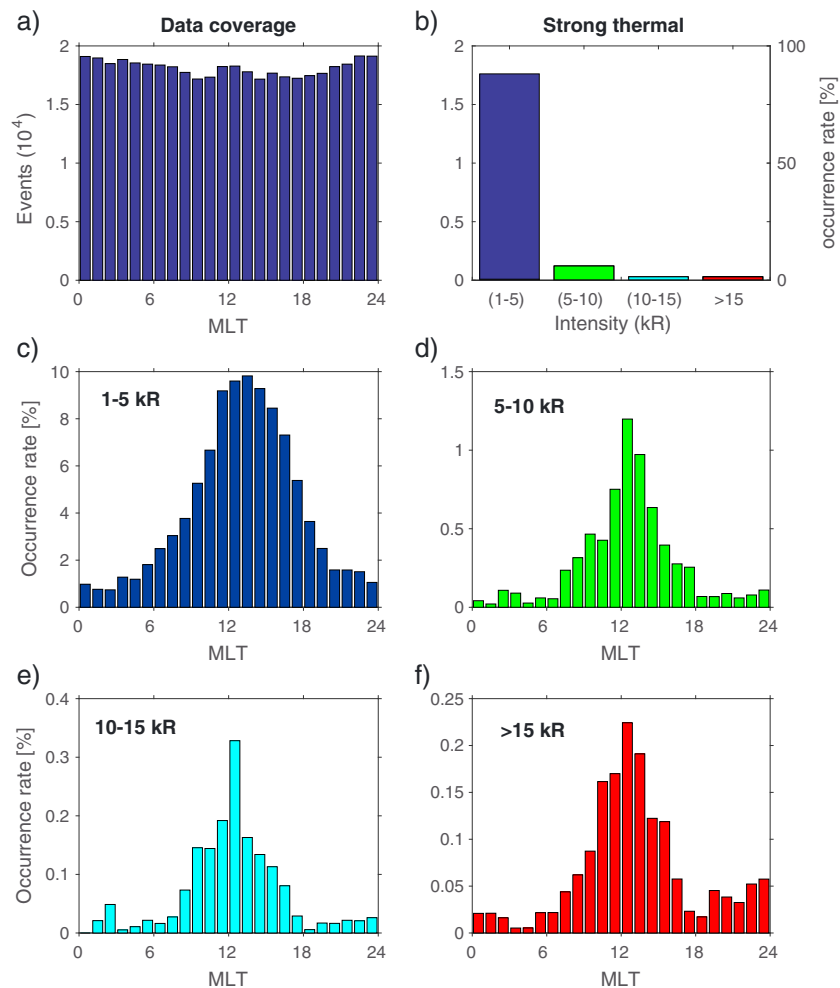
Figure 1. (a) Data coverage for the study with respect to magnetic local time. The data consists of ESR 42 m experiments that ran continuously for approximately 24 h during the years 2000–2015. (b) The occurrence rate of different intensity categories of 1–5, 5–10, 10–15, and >15 kR and the vertical axis on the left shows the number of events, while that on the right shows the occurrence rate in percentage. The magnetic local time distribution of the intensity categories for (c) 1–5, (d) 5–10, (e) 10–15, and (f) >15 kR, respectively. The vertical axes show the occurrence rate.

The "strong thermal" refers to all results which give a total intensity of 1 kR or more, whereas the "weak thermal" refers to all the remaining data (i.e., with a total intensity less than 1 kR).

Chamberlain (1961) described typical intensity levels as 250 R for airglow and 1 kR for aurora emissions. The 1 kR has since been used in studies as a threshold for emissions generally assumed to be associated with direct impact excitation by precipitating particles (e.g., Frank & Craven, 1988; Kamide et al., 1999; Sims et al., 2012). In addition, the distributions of ionospheric parameters were almost the same when the threshold was raised above 1 kR but varied when lower thresholds were used. In our study, the focus is on the strong thermal component, and we consider the thermal excitation to be significant if it exceeds the airglow intensity levels and produces aurora intensity levels. For this reason we use a 1 kR threshold to separate out the strong thermal component.

We further analyze the ionospheric, solar wind and interplanetary magnetic field parameters during the two categories and for different magnetic local times (MLT).

3. Observations and Results

A general overview of the data used in the study is presented in Figure 1. Figure 1a shows the magnetic local time distribution of the data coverage. There is a relatively even distribution at all magnetic local times. In addition to the data coverage in Figure 1a, the distribution of the strong thermal component intensities is shown
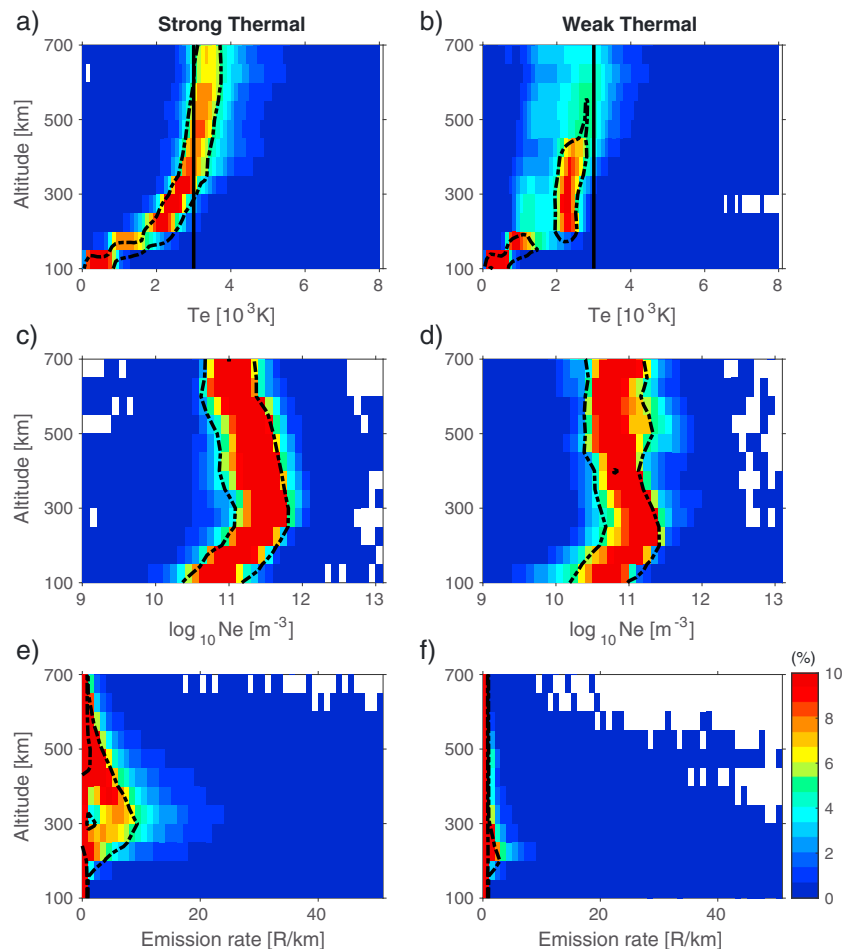
Figure 2. Distribution of electron temperature (T_e), electron density (N_e), and the calculated volume emission rate of the thermally excited 630.0 nm, respectively, normalized at each altitude step. (a, c, and e) The parameters associated with the strong thermally excited emission (>1 kR). (b, d, and f) The parameters associated with the weak thermally excited emissions (<1 kR). The color bar indicates the relative distribution in percentage. The black dotted line marks the 5% level. The black vertical lines in Figures 2a and 2b mark 3000 K.

in Figure 1b. The bins in Figure 1b contain data points with intensities 1–5, 5–10, 10–15, and >15 kR from left to right, respectively. Each bin in Figures 1a and 1c–1f contains data points for 1 h MLT. Figure 1b shows that the 1–5 kR bin contains ~85% of the strong thermal component. The MLT distribution of the intensity bins in Figure 1b is given in Figures 1c–1f, respectively. From Figure 1c which is representative of the strong thermal component, we see that generally, the occurrence rate is higher on the dayside (06:00–18:00 MLT) compared to the nightside (18:00–06:00). The peak occurrence rate is observed near magnetic noon, where ~10% of the data have a strong thermal component, which is 10 times higher than the occurrence rate found on the nightside. All the intensity categories show a similar MLT distribution with the 1–5 kR as the dominant intensity level.

We now analyze the distributions of measured electron temperature, density, and calculated thermal excitation rates at different altitudes. Figure 2 shows the distribution of electron temperature (T_e), electron density (N_e), and volume emission rate normalized at each 50 km altitude step, for the strong thermal events (a, c, e) and weak thermal events (b, d, f). The black dotted line marks the 5% level of the distribution, while the vertical black lines in Figures 2a and 2b mark 3000 K. The electron temperature is generally low at the low altitudes for both weak and strong thermal component (Figures 2a and 2b) distributions, and both distributions are similar. At higher altitudes (>250 km), however, the two distributions become different with the weak thermal component temperature mainly remaining low (below 3000 K) and the strong thermal component temperature exceeds 3000 K. Similarly, there is no big difference in the electron density at low altitudes, but at higher altitudes, the electron density associated with the strong thermal component is generally higher than that
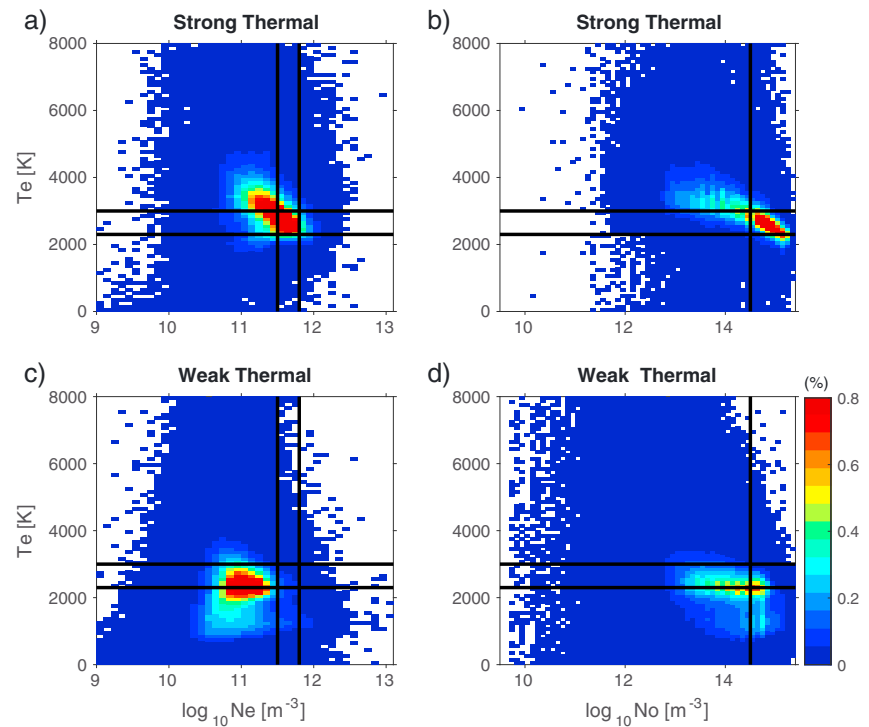
Figure 3. Distribution of densities associated with the strong and weak thermal populations at different electron temperatures. (a and c) The electron density distributions. (b and d) The modeled neutral atomic oxygen densities. The two vertical lines in Figures 3a and 3c mark electron density 5×10^{11} and 8×10^{11} m^{-3}, respectively, while that in Figures 3b and 3d marks atomic oxygen number density 5×10^{14} m^{-3}. The two horizontal lines mark electron temperature 2300 and 3000 K, respectively, in all the panels. The color bar shows the distribution in percentage.

associated with the weak thermal component population. The derived thermal excitation emission rates are shown in Figures 2e and 2f. This was calculated for both weak and strong thermal distributions in order to get a general picture and comparison between the two. From the presented weak thermal component distribution (Figure 2f), we notice that the peak occurrence rate is at less than 1 R/km at all altitudes, and the distribution generally extends to 5 R/km. On the other hand, the strong thermal emission rate distribution (Figure 2e) below 250 km is less than 1 R/km as well but it is enhanced at altitudes above 250 km. The highest emission rate is found at 300–350 km altitude for the strong thermal component.

The distribution of the electron and modeled atomic oxygen densities at different electron temperatures for both strong and weak thermal populations is presented in Figure 3. The color bar gives the distribution in percentage. The black horizontal lines mark the 2300 and 3000 K electron temperatures. The two vertical lines in Figures 3a and 3c mark electron density 5×10^{11} and 8×10^{11} m^{-3}, respectively, while that in Figures 3b and 3d marks atomic oxygen number density 5×10^{14} m^{-3}, respectively. The peak population is found between 2300 and 4000 K for electron density, and the model suggests that the peak population for the neutral atomic oxygen is only between 2300 and 3000 K for the strong thermal component distributions (Figures 3a and 3b). The peak population we find below 3000 K is unexpected. On comparison with the weak thermal component distribution, both the electron and modeled neutral atomic oxygen densities peak at relatively lower densities and electron temperatures compared to the strong thermal component distribution. When we normalize the densities at each electron temperature step, we get the distributions in Figure 4. The region with the peak populations in the strong thermal distributions just show very low occurrence in the weak thermal distributions, particularly for the regions enclosed by all the four (three) lines in the four panels.

Figure 5 shows the probability of having strong thermally excited emissions given the different electron temperature, density, atomic oxygen density, emission rates, and altitudes. The two horizontal lines mark the same temperatures as in the previous two figures. The same temperature levels are marked by the vertical lines in Figure 5c. Generally, Figure 5 shows the probability for strong thermally excited emissions to occur
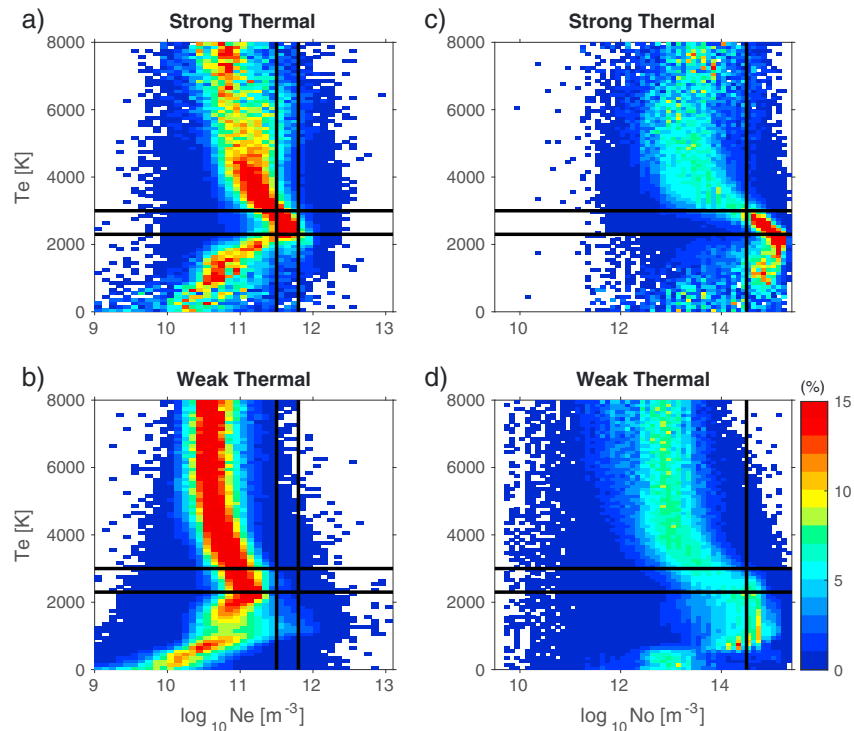
Figure 4. Normalized distribution of (a, c) electron density and (b, d) modeled neutral atomic oxygen density in each electron temperature step. The two vertical lines in Figures 4a and 4c mark electron density 5×10^{11} and 8×10^{11} m^{-3}, respectively, while that in Figures 4b and 4d marks atomic oxygen number density 5×10^{14} m^{-3}. The two horizontal lines mark electron temperature 2300 and 3000 K, respectively, in all the panels. The color bar shows the distribution in percentage.

to be high when electron temperature exceeds 2300 K, electron density exceeds 2×10^{11}, and the model suggests neutral atomic oxygen density exceeding 1×10^{14} m^{-3} for altitudes above 250 km.

We now analyze the prevailing interplanetary magnetic field and solar wind conditions during the strong thermally excited emissions which are then compared to the occurrence for the full data set. Figure 6 shows the occurrence rate of IMF B_y, B_z, and B_x for the full data set (a, c, e). Figures 6b, 6d, and 6f show the percentage of the full data set (a, c, e) which is simultaneous with a strong thermal component in the ionosphere. Of the simultaneous IMF components, negative B_z shows the highest occurrence rate (see Figure 6d) while the positive B_z shows a higher occurrence rate than the near-zero values. There is no difference in occurrence rate seen in the different configurations of B_x. Also, nonzero B_y shows a higher occurrence rate compared to the near-zero B_y. Figure 7 has the same structure as Figure 6 but instead shows the solar wind parameters: solar wind density, speed, and dynamic pressure, from top to bottom, respectively. For these solar wind parameters, the relatively high dynamic pressure shows the highest occurrence rate (see Figure 7f) followed by the high solar wind density and solar wind speed.

4. Discussion

A few case studies on thermal excitation have been done in the past. In some studies thermal excitation has been suggested as the possible source for observed emissions, whereas other theoretical studies have provided theoretical explanations for the same process. Intense 630.0 nm emissions associated with enhanced electron temperature and density have been reported at high latitudes centered at magnetic noon, since four decades ago (e.g., Shepherd, 1979). In efforts of understanding these emissions, Wickwar and Kofman (1984) investigated and calculated the thermal component during the periods of enhanced electron temperature and found that thermal excitation dominated the production of the 630.0 nm emission. However, due to the sunlit conditions, they lacked optical data for comparison. Later, Carlson et al. (2013) reported detection of thermal 630.0 nm emissions in the cusp using time/space agreement between calculations and observations. Using the same formulae, Kwagala et al. (2017) presented a direct comparison between the calculations and
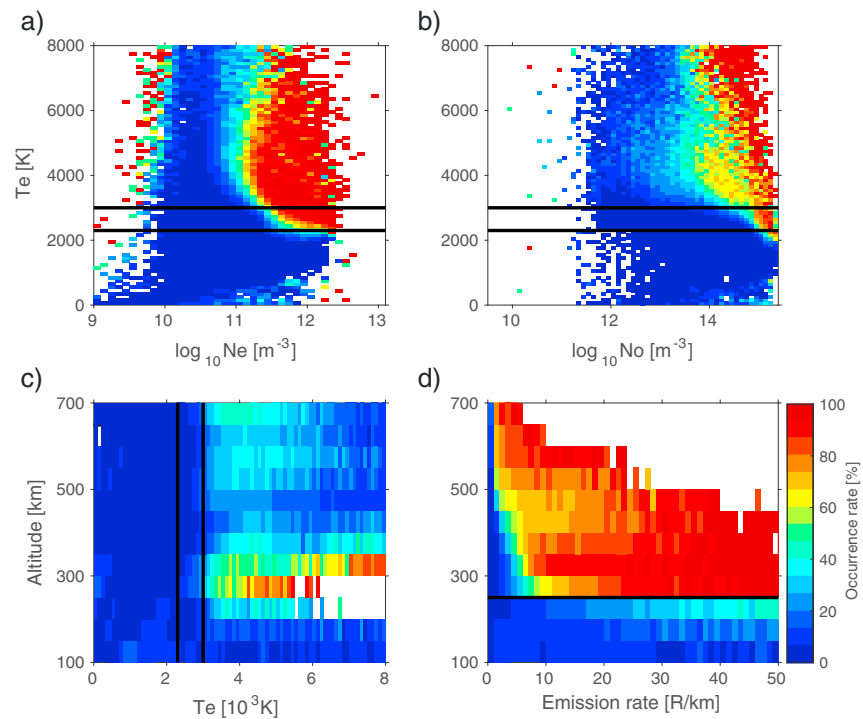
Figure 5. Occurrence rate of the strong thermally excited emissions at different electron temperatures, densities, modeled neutral atomic oxygen densities, emission rates, and altitudes. Electron temperature versus density for (a) electrons and (b) atomic oxygen. (c, d) Occurrence rate at different electron temperatures and emission rates at different altitudes. The vertical lines in Figure 5c mark electron temperatures 2300 and 3000 K. In Figures 5a and 5b, the horizontal lines mark electron temperatures 2300 and 3000 K, respectively, while that in Figure 5d marks the 250 km altitude. The color bar shows the occurrence rate.

the optical observations. All these case studies suggest that the thermal component can be dominant at the polar latitudes. Not until the present study has anyone carried out an extensive study on the thermal excitation involving large data sets. The availability of current state-of-the-art ground-based instrumentation on Svalbard has provided the possibility for our study. We now discuss the results presented in the previous section with focus on the strong thermal component.
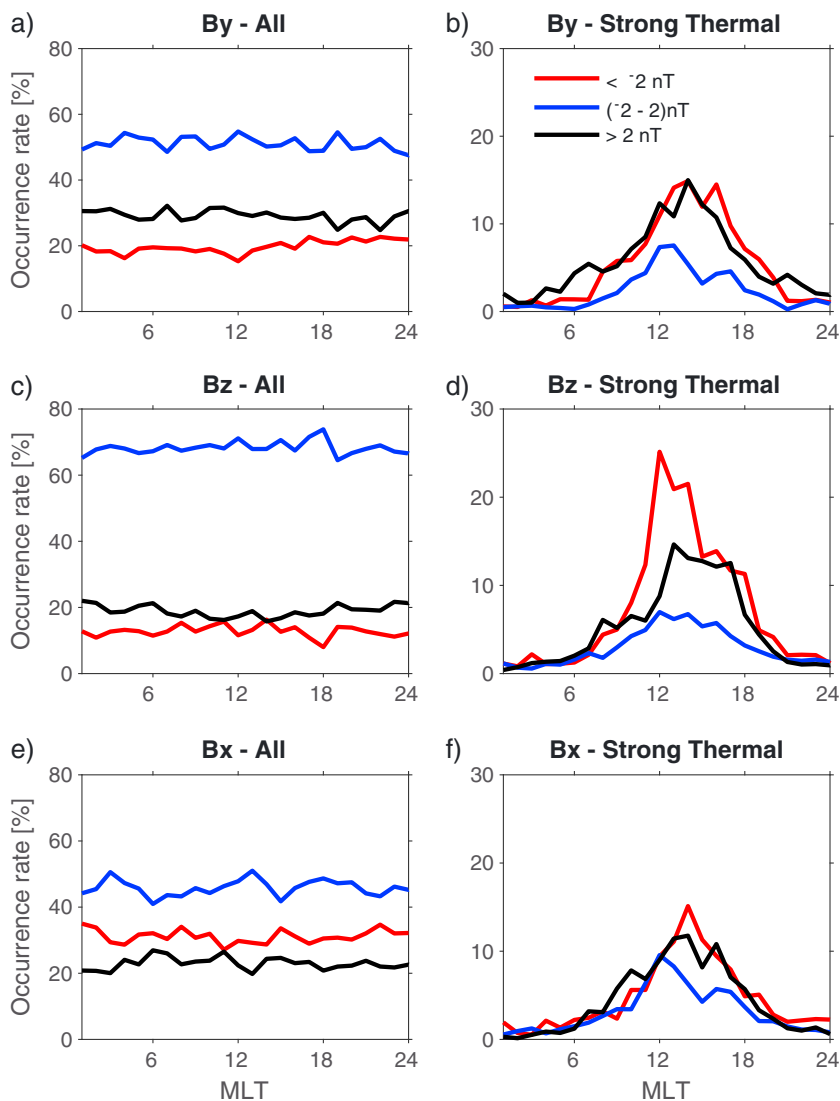
4.1. MLT Distribution

Statistically, our study records a peak occurrence around magnetic noon and generally a higher occurrence on the dayside by a factor of 10 than on the nightside. Based on a statistical study, Zhou et al. (2000) reported the cusp to be located between 0800 and 1600 MLT, which is coincident with the highest occurrence rate in our study. This also backs up the fact that all the cases reported in literature (e.g., Carlson et al., 2013; Kwagala et al., 2017; Wickwar & Kofman, 1984) were in the cusp region, since our results suggest higher probability of such events at this location compared to the other magnetic local times. This may also be linked to the difference between the typical average energies of precipitating electrons on the nightside and dayside in the polar ionosphere, which are hard and soft, respectively (e.g., Newell et al., 2004). Although the cusp does not extend over the whole dayside where we see a relatively high occurrence rate, the magnetic merging exists throughout the dayside magnetopause and not only in the region that produces the cusp precipitation (Lockwood, Denig, et al., 1993; Newell et al., 2004).

4.2. Ionospheric Conditions
4.2.1. Prevailing Conditions

From the observations in the previous section, the electron density and temperature distributions are shown to differ between the strong and weak thermal components. We can take the weak thermal data as a representation of the average ionosphere when the contribution thermal excitation is insignificant and refer to it as the average ionosphere. Our observations show the peak occurrence rate of the strong thermal component to occur at electron temperatures 2300–4200 K (see Figures 3 and 4). According to literature, we would expect the lower limit to be ∼3000 K. For the purposes of our discussion, we divide the temperature range
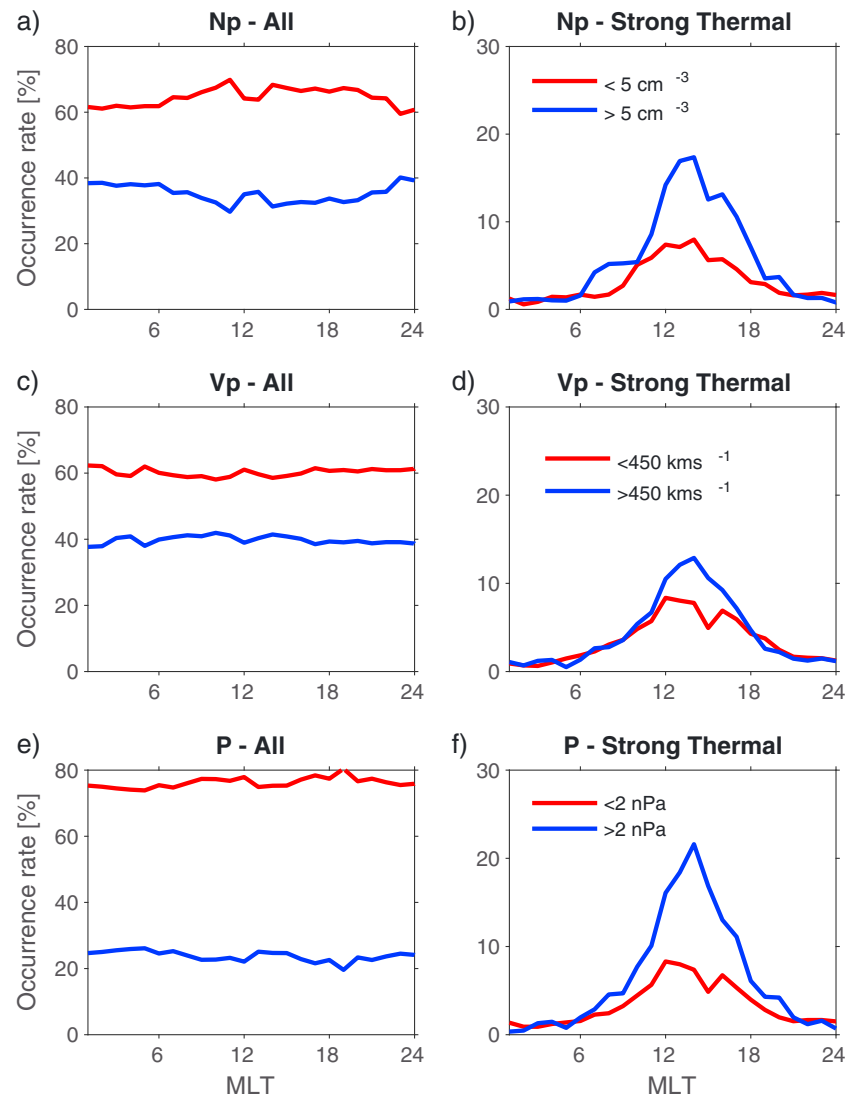
Figure 6. MLT distribution of the interplanetary magnetic field parameters B_y, B_z, and B_x. (a, c, and e) The distribution for the whole data set. (b, d, and f) The percentage of the IMF component occurring at the same time as the strong thermal component in the ionosphere. The vertical axes show the occurrence rate in percentage.

into two categories and use terms lower and high to extreme to refer to temperature ranges 2300–3000 and >3000 K, respectively. We also use terms typical and extreme for the associated electron density levels of 2×10^{11} and $>5 \times 10^{11}$ m^{-3}, respectively. With this in mind, looking at the electron temperature distribution in Figure 2, we find that above 250 km altitude, the electron temperatures associated with strong thermally excited emissions generally exceed those of the average ionosphere. At these altitudes, our results show that the strong thermal component is associated with high to extreme electron temperatures. These temperatures are in agreement with literature (e.g., Carlson, 1998; Carlson et al., 2013; Johnsen et al., 2012; Kozyra et al., 1990; Kwagala et al., 2017; Lockwood, Carlson, & Sandholt, 1993; Wickwar & Kofman, 1984), which suggests 3000 K as a key temperature for thermal emissions to become important. It is expected that at this temperature, the energy distribution of the electron gas can have high enough number of electrons in its high-energy tail to excite atomic oxygen to ^{1}D state.

However, we also observe a new population where an outstanding high occurrence of strong thermal emissions is present, at lower electron temperatures for extreme electron densities. The empirical atmospheric model suggests that this new population is associated with enhanced neutral atomic oxygen densities. The peak occurrence at extreme neutral atomic oxygen densities for lower electron temperatures in the strong

Figure 7. MLT distribution of solar wind parameters solar wind density, speed, and dynamic pressure. (a, c, and e) The distribution for the whole data set. (b, d, and f) The percentage of the solar wind parameters occurring at the same time as the strong thermal component in the ionosphere. The vertical axes show the occurrence rate in percentage.

thermal component distribution is absent in a similar distribution for the weak thermal. Generally, the rest of the model atomic oxygen densities are more evenly distributed over the different electron temperatures. There is a possibility that the generation mechanisms for the lower electron temperatures are different from those of the extreme electron temperatures. In both cases the electron density plays an equal role.

4.2.2. Electron Thermal Balance

The electron temperature in the ionosphere is determined by a thermal balance between heating and cooling rates. The heating and cooling processes in the ionosphere are equally important. Generally, the heating of the electrons is dominated by collisions between thermal and photoelectrons, which is proportional to the electron density. The electron thermal balance gets more complicated at the polar and high latitudes. There are additional heat sources like the particle precipitation and frictional heating due to the convective plasma in the polar cap which leads to frictional heating for ions which transfer part of the heat to the electrons (Schunk & Nagy, 1978). The electron gas is normally expected to cool by collisions with ambient neutrals for altitudes below 200 km and with ambient ions at higher altitudes (Brace & Theis, 1978; Kozyra et al., 1990; Schunk & Nagy, 1978; Su et al., 2015). Our study focusses on the higher altitudes and therefore interested in the latter cooling process which is proportional to the square of the electron density (Brace & Theis, 1978; Kozyra et al., 1990; Schunk & Nagy, 1978). Therefore, the ionosphere is expected to be in good thermal contact

whenever the electron density is high. Several studies have reported the expected negative correlation between the electron density and electron temperature in the ionosphere (e.g., Brace & Theis, 1978; Bilitza, 1975; Bilitza et al., 2007; Su et al., 2015).

However, a positive correlation has also been reported in some literature (e.g., Bilitza et al., 2007). Since a positive correlation implies that the heating increases more rapidly than the electron density, an additional heat source might be required to fully account for the positive correlation (Kakinami et al., 2011). In our results (Figures 2a and 2c), we observe a high occurrence for electron temperatures of 3000 K and electron density above 10^{11} m^{-3}. This could be a positive correlation between electron temperature and density. If so, it would indicate a faster heating rate than the cooling. Carlson et al. (2013) suggests that when the ion-electron collisions are not fast enough, to achieve a thermal balance at higher electron temperatures, the electron gas cools via collisions with neutral atomic oxygen, exciting it to the ^{1}D state which deexcites by emission of 630.0 nm photons. This gives rise to the thermally excited emissions which have been reported in the polar and high-latitude ionosphere (e.g., Carlson, 1998; Carlson et al., 2013; Johnsen et al., 2012; Kwagala et al., 2017; Wickwar & Kofman, 1984).

The ^{1}D can, however, be quenched mainly by collisions with molecular nitrogen. The amount of 630.0 nm emission from thermal excitation is dependant on the neutral atmosphere densities of atomic oxygen and molecular nitrogen in addition to the electron density and temperature. Significant 630.0 nm emissions only arise at altitudes where the molecular nitrogen is infrequent. Above 250 km altitude, the molecular nitrogen density decreases significantly with altitude and the lighter atomic oxygen dominates. So in our work we consider the quenching to be negligible.

4.3. Likely Driving Mechanism

Dayside magnetopause reconnection has been reported to be characterized by nonzero IMF B_z (e.g., Trattner et al., 2007), high solar wind dynamic pressure (e.g., Fuselier et al., 2000), and enhanced ionospheric electron temperature in the ionosphere (e.g., Lockwood, Denig, et al., 1993). Our results show to a great extent these characteristics, hence indicating dayside magnetopause reconnection as a possible major driving mechanism responsible for the heating of ambient electrons in the ionosphere. Also, the high occurrence rate shown for the high solar wind density could imply increase in the magnetosheath density which on magnetic reconnection would lead to high number flux of soft precipitation in the cusp. The increase in number flux of soft precipitation implies more Coulomb collisions with the ambient electrons in the ionospheric cusp which increase the electron temperature and hence the occurrence of thermal emissions. In addition, our results suggest a strong association of the strong thermal component to the cusp signature in the ionosphere. For example, we find a strong similarity between the cusp signatures in the ionosphere reported by Nilsson et al. (1996) and the ionospheric condition we observe where there is a high occurrence rate. Vontrat-Reberac et al. (2001) estimated that the cusp electron precipitations heat the ambient electron gas to much higher temperatures compared to precipitations from other source regions. Further, Newell et al. (2004) report a 35% (25%) of the dayside merging to occur in the cusp for the southward (northward) IMF, respectively. On comparison, our study shows a possible 25% (15%) peak occurrence rate for the southward (northward) IMF configurations around magnetic noon. This could imply one of two conditional situations: either (1) if all the strong thermally exited emissions (at peak |Bz|) result from dayside merging, then 25% (15%) of southward (northward) dayside merging ends in strong thermal emission, or (2) if all strong thermal emissions arise from the cusp, then ~10% of it does not give rise to strong thermal emissions (i.e., ~ 90% of the cusp precipitation ends up in strong thermal emissions). Provided that the 630.0 nm emissions in the cusp arise from thermal excitation versus direct electron impact excitation, then we agree with earlier studies that the role of transient magnetopause reconnection in driving the global ionospheric convection could be greater than earlier anticipated (Carlson, 1998; Carlson et al., 2013; Kwagala et al., 2017; Lockwood, Carlson, & Sandholt, 1993).

4.3.1. Peak Emission Altitude

Provided that the electron precipitation from the dayside magnetic reconnection is the heating source of the electron gas in the polar ionosphere, the emission altitude of the 630.0 nm emissions has been associated with the amount of energy entering the ionosphere (Lockwood, Carlson, & Sandholt, 1993). For example, the authors point out that if the peak emission altitude doubled, it could imply that the entry area of the energy is bigger by an order of 4. Based on the distribution of emission rates at different altitude in Figure 2e, we note that the peak for the strong thermal emission is in the 300–350 km bin. This is very similar to the emission rates' altitudes in the model presented by Johnsen et al. (2012, Figure 6), where the peak volume emission rate

for thermal excitation was at ~350 km altitude. This peak emission altitude (~350 km) for thermally excited emission also agrees with other studies (e.g., Egeland et al., 1992; Kwagala et al., 2017; Wickwar and Kofman, 1984), however, a little lower than 400–500 km from some studies (e.g., Carlson et al., 2013; Kozyra et al., 1990).

4.4. Potential Driving Mechanisms

From the above discussion, our results suggest that the ambient electrons are, to a large extent, heated by particle precipitation originating from dayside magnetic reconnection. However, this is not the only driving process for thermal excitation in the upper polar ionosphere. Other processes, like vertical/horizontal transport and waves, could also be driving the thermal emissions as well. At midlatitudes, traveling ionospheric disturbances which are the atmospheric gravity waves' signature in the ionosphere have been reported to increase the electron density by an order of 2–4 but decrease the electron temperature by ~40% (e.g., Huang et al., 2005). With such low electron temperatures we can rule out gravity waves, and most of the horizontal transports have the same effect on electron temperature (e.g., Liu et al., 2016, and references therein). However, wave-particle interaction like the thermomagnetic mechanism described by Kagan et al. (1996) could be a potential mechanism leading to thermal excitation. On the other hand, vertical transport may potentially contribute to the heating of ambient electrons in the polar ionosphere. For example, downward heat flow in the polar cap has been reported to heat the ambient electron gas to high temperature on the nightside (e.g., David et al., 2011), however, above 800 km altitude. Our study does not go into details of these possible driving processes. Kwagala et al. (2017) also reported significant thermal component during upwelling (e.g., Ronksley, 2016; Sojka et al., 2001) for one of their case studies.

4.4.1. Neutral Upwelling

There seems to be an association between thermal excitation and neutral upwelling or density enhancements in the cusp and polar ionosphere. The neutral upwelling is believed to lead to neutral density enhancements at high altitudes, and the first observations of this were reported by Lühr et al. (2004). Soft particle precipitation from magnetic reconnection has been suggested as a major driving mechanism of upwelling (e.g., Carlson et al., 2012; Horvath & Lovell, 2017; Lühr et al., 2004; Schlegel et al., 2005). Our results also suggest the same driving mechanism for the strong thermally exited emissions. Particularly, the atomic oxygen density enhancement suggested by the model at the lower electron temperatures could indicate neutral upwelling during strong thermally excited emissions. Whether the two processes just happen to occur at the same time, or one leads to another, that remains unclear.

4.5. Assumptions and Limitations

We now discuss the uncertainty and assumptions associated with and made in our study. We used an empirical atmospheric model to derive the atomic oxygen number density. The NRLMSISE-00 model estimates the neutral number density by interpolating and extrapolating data sets for periods and geophysical conditions that are not covered by the available database which includes ground-based, rocket, and satellite measurements. Therefore, we use the model because we have no measurements of the atomic density and also neutral constituents in the thermosphere are believed to vary quite uniformly compared to their charged counterparts. However, the model is not always accurate but remains a statistical average although the database now includes more data covering extreme locations and forcing (Picone et al., 2002). Some studies have reported underestimates of 20–30% during an active high-latitude ionosphere (e.g., Forbes et al., 2005; Liu & Lühr, 2005). When Kwagala et al. (2017) accounted for the 30% underestimate, the calculated thermal component increased by 10–15% and therefore concluded that the neutral density from the model gives a lower limit of the thermal component. On a general view of the NRLMSISE-00 model compared to the other atmospheric models, Pardini et al. (2012) investigated uncertainty and bias in upper atmosphere models during the solar cycle 23 and found that the NRLMSISE-00 model had the minimum biases at all altitudes among the models that were analyzed. We therefore believe that the NRLMSISE-00 model is one of the best we could use to get the atomic oxygen density. Another model that can be used for the same purpose is the National Center for Atmospheric Research thermosphere-ionosphere-electrodynamic general circulation model (NCAR/TIE-GCM) (Qian et al., 2009, 2014; Richmond et al., 1992). We plan to look at TIE-GCM simulations in the future.

We specifically use the stationary radar beam (i.e., a fixed observation geometry), and therefore, all our data comes from a fixed area in magnetic latitude. With the 1–2 min data postintegration time, we assume that the emitting oxygen atoms and the ambient electrons remain in the same integrated area. The lifetime of the 630.0 nm emissions, which is ~110 s (Rees & Roble, 1975), is in the same ballpark as the postintegration time of the radar data (see Table 1). We further point out that the cusp is not always above Svalbard. The location

of the cusp with respect to Svalbard is believed to be dependant on the IMF B_z configuration. When B_z is southward, then the cusp is south and more likely to be in the ESR beam; on the other hand, when the IMF is northward, the cusp most likely moves north of Svalbard, out of the ESR beam (Sandholt et al., 1998). In a statistical study on the location of the open/closed boundary, Johnsen and Lorentzen (2012) showed that the cusp would be located north of the ESR beam half of the time. For this reason, not all strong thermal emissions observed around magnetic noon will necessarily be from the cusp precipitation. Thermal excitation which leads to strong thermal emissions could be occurring outside the ESR beam as well.

5. Summary and Conclusion

We have carried out the first statistical study of thermally excited emissions based on the ESR radar measurements from the years of 2000–2015. Our study agrees with literature on the ionospheric conditions necessary for the thermally excited emissions. These conditions require the electron temperature to exceed 3000 K and electron density of $(1-5) \times 10^{11}$ m^{-3} for the thermal component to be important, which we find in our study as well. However, we report a new population at relatively lower temperatures between 2300 and 3000 K when the electron density is relatively enhanced $(5-8) \times 10^{11}$ m^{-3}. This could be associated with neutral upwelling or density enhancement since the neutral atmosphere model suggests that the neutral atomic oxygen density is enhanced during this new population. It remains unclear what the connection between neutral upwelling and thermal excitation is. In conclusion, we strongly recommend that all studies involving dayside 630.0 nm emissions and thermal balance in the polar and cusp ionosphere should take into account thermal excitation.

References

Bilitza, D. (1975). Models for the relationship between electron density and temperature in the upper ionosphere. *Journal of Atmospheric and Terrestrial Physics*, 37(9), 1219–1222. https://doi.org/10.1016/0021-9169(75) 90193-2

Bilitza, D., Truhlik, V., Richards, P., Abe, T., & Triskova, L. (2007). Solar cycle variations of mid-latitude electron density and temperature: Satellite measurements and model calculations. *Advances in Space Research*, 39(5), 779–789. https://doi.org/10.1016/j.asr.2006.11.022

Brace, L. H., & Theis, R. F. (1978). An empirical model of the interrelationship of electron temperature and density in the daytime thermosphere. *Geophysical Research Letters*, 5(4), 275–278. https://doi.org/10.1029/GL005i004p00275

Carlson, H. C. (1998). Response of the polar cap ionosphere to changes in (Solar Wind) IMF. In J. Moen, A. Egeland, & M. Lockwood (Eds.), *Polar cap boundary phenomena* (Vol. 509, pp. 255–270). Netherlands, Dordrecht: Springer. https://doi.org/10.1007/978-94-011-5214-3-19

Carlson, H. C., Spain, T., Aruliah, A., Skjaeveland, A., & Moen, J. (2012). First-principles physics of cusp/polar cap thermospheric disturbances. *Geophysical Research Letters*, 39, L19103. https://doi.org/10.1029/2012GL053034

Carlson, H. C., Oksavik, K., & Moen, J. I. (2013). Thermally excited 630.0 nm O (1D) emission in the cusp: A frequent high-altitude transient signature. *Journal of Geophysical Research: Space Physics*, 118, 5842–5852. https://doi.org/10.1002/jgra.50516

Chamberlain, J. W. (1961). Chapter 9. The airglow spectrum. In J. W. Chamberlain (Ed.), *Physics of the Aurora and Airglow, International Geophysics* (pp. 345–392). New York: Academic Press. https://doi.org/10.1016/S0074-6142(08)60657-9

David, M., Schunk, R., & Sojka, J. (2011). The effect of downward electron heat flow and electron cooling processes in the high-latitude ionosphere. *Journal of Atmospheric and Solar-Terrestrial Physics*, 73(16), 2399–2409. https://doi.org/10.1016/j.jastp.2011.08.009

Doering, J., & Gulcicek, E. (1989). Absolute differential and integral electron excitation cross sections for atomic oxygen.7. The ^{3}P→^{1}D and ^{3}P→^{1}S transitions from 4.0 to 30 eV. *Journal of Geophysical Research*, 94, 1541–1546. https://doi.org/10.1029/JA094iA02p01541

Egeland, A., Carlson, H. C., Denig, W. F., Fukui, K., & Weber, E. (1992). Day-side auroral signatures based on simultaneous, coordinated observations at Svalbard and Greenland. *IEEE Transactions on Plasma Science*, 20(6), 726–739. https://doi.org/10.1109/27.199521

Forbes, J. M., Lu, G., Bruinsma, S., Nerem, S., & Zhang, X. (2005). Thermosphere density variations due to the 15–24 April 2002 solar events from CHAMP/STAR accelerometer measurements. *Journal of Geophysical Research*, 110, A12S27. https://doi.org/10.1029/2004JA010856

Frank, L. A., & Craven, J. D. (1988). Imaging results from Dynamics Explorer 1. *Reviews of Geophysics*, 26(2), 249–283. https://doi.org/10.1029/RG026i002p00249

Fuselier, S. A., Trattner, K. J., & Petrinec, S. M. (2000). Cusp observations of high- and low-latitude reconnection for northward interplanetary magnetic field. *Journal of Geophysical Research*, 105(A1), 253–266. https://doi.org/10.1029/1999JA900422

Henry, R., Burke, P., & Sinfailam, A.-L. (1969). Scattering of electrons by C, N, O, N$^+$, O$^+$, and O^{++}. *Physical Review*, 178, 218–225. https://doi.org/10.1103/PhysRev.178.218

Horvath, I., & Lovell, B. C. (2017). Investigating the polar ionosphere during the development of neutral density enhancements on 24–25 September 2000. *Journal of Geophysical Research: Space Physics*, 122(4), 4600–4616. https://doi.org/10.1002/2016JA023799

Huang, C.-S., Foster, J. C., Goncharenko, L. P., Erickson, P. J., Rideout, W., & Coster, A. J. (2005). A strong positive phase of ionospheric storms observed by the Millstone Hill incoherent scatter radar and global GPS network. *Journal of Geophysical Research*, 110, A06303. https://doi.org/10.1029/2004JA010865

Johnsen, M. G., & Lorentzen, D. A. (2012). A statistical analysis of the optical dayside open/closed field line boundary. *Journal of Geophysical Research*, 117, A02218. https://doi.org/10.1029/2011JA016984

Johnsen, M. G., Lorentzen, D. A., Holmes, J. M., & Løvhaug, U. P. (2012). A model based method for obtaining the open/closed field line boundary from the cusp auroral 6300 Å[OI] red line. *Journal of Geophysical Research*, 117, A03319. https://doi.org/10.1029/2011JA016980

Kagan, L. M., Kelley, M. C., & Doe, R. A. (1996). Ionospheric electron heating by structured electric fields: Theory and experiment. *Journal of Geophysical Research*, 101, 10,893–10,907. https://doi.org/10.1029/96JA00298

Kakinami, Y., Watanabe, S., Liu, J.-Y., & Balan, N. (2011). Correlation between electron density and temperature in the topside ionosphere. *Journal of Geophysical Research*, 116, A12331. https://doi.org/10.1029/2011JA016905

Kamide, Y., Kokubun, S., Bargatze, L., & Frank, L. (1999). The size of the polar cap as an indicator of substorm energy. *Physics and Chemistry of the Earth*, 24, 119–127.

Kozyra, J. U., Valladares, C. E., Carlson, H. C., Buonsanto, M. J., & Slater, D. W. (1990). A theoretical study of the seasonal and solar cycle variations of stable aurora red arcs. *Journal of Geophysical Research*, *95*(A8), 12,219–12,234. https://doi.org/10.1029/JA095iA08p12219

Kwagala, N. K., Oksavik, K., Lorentzen, D. A., & Johnsen, M. G. (2017). On the contribution of thermal excitation to the total 630.0 nm emissions in the northern cusp ionosphere. *Journal of Geophysical Research: Space Physics*, *122*, 1234–1245. https://doi.org/10.1002/2016JA023366

Lan, V. K., Feautrier, N., Dourneuf, M. L., & Regemorter, H. V. (1972). Cross sections calculations for electron oxygen scattering using the polarized orbital close coupling theory. *Journal of Physics B: Atomic and Molecular Physics*, *5*(8), 1506–1516.

Lehtinen, M. S., & Huuskonen, A. (1996). General incoherent scatter analysis and GUISDAP. *Journal of Atmospheric and Terrestrial Physics*, *58*(1), 435–452. https://doi.org/10.1016/0021-9169(95)00047-X

Link, R. (1982). Dayside magnetospheric cleft auroral processes (PhD Thesis). Canada: York University.

Liu, H., & Lühr, H. (2005). Strong disturbance of the upper thermospheric density due to magnetic storms: CHAMP observations. *Journal of Geophysical Research*, *110*, A09S29. https://doi.org/10.1029/2004JA010908

Liu, J., Wang, W., Burns, A., Solomon, S. C., Zhang, S., Zhang, Y., & Huang, C. (2016). Relative importance of horizontal and vertical transports to the formation of ionospheric storm-enhanced density and polar tongue of ionization. *Journal of Geophysical Research: Space Physics*, *121*, 8121–8133. https://doi.org/10.1002/2016JA022882

Lockwood, M., Carlson, H. C., & Sandholt, P. E. (1993). Implications of the altitude of transient 630-nm dayside auroral emissions. *Journal of Geophysical Research*, *98*(A9), 15,571–15,587. https://doi.org/10.1029/93JA00811

Lockwood, M., Denig, W., Farmer, A., Davda, V., Cowley, S., & Lühr, H. (1993). Ionospheric signatures of pulsed reconnection at the Earth's magnetopause. *Nature*, *361*(6411), 424–428.

Lühr, H., Rother, M., Köhler, W., Ritter, P., & Grunwaldt, L. (2004). Thermospheric up-welling in the cusp region: Evidence from CHAMP observations. *Geophysical Research Letters*, *31*, L06805. https://doi.org/10.1029/2003GL019314

Mantas, G. P., & Carlson, H. C. (1991). Reexamination of the O(3P→1D) excitation rate by thermal electron impact. *Geophysical Research Letters*, *18*(2), 159–162. https://doi.org/10.1029/91GL00019

Newell, P. T., Ruohoniemi, J. M., & Meng, C.-I. (2004). Maps of precipitation by source region, binned by IMF, with inertial convection streamlines. *Journal of Geophysical Research*, *109*, A10206. https://doi.org/10.1029/2004JA010499

Nilsson, H., Yamauchi, M., Eliasson, L., Norberg, O., & Clemmons, J. (1996). Ionospheric signature of the cusp as seen by incoherent scatter radar. *Journal of Geophysical Research*, *101*(A5), 10,947–10,963. https://doi.org/10.1029/95JA03341

Pardini, C., Moe, K., & Anselmo, L. (2012). Thermospheric density model biases at the 23rd sunspot maximum. *Planetary and Space Science*, *67*(1), 130–146. https://doi.org/10.1016/j.pss.2012.03.004

Picone, J. M., Hedin, A. E., Drob, D. P., & Aikin, A. C. (2002). NRLMSISE-00 empirical model of the atmosphere: Statistical comparisons and scientific issues. *Journal of Geophysical Research*, *107*(A12), 1468. https://doi.org/10.1029/2002JA009430

Qian, L., Solomon, S. C., & Kane, T. J. (2009). Seasonal variation of thermospheric density and composition. *Journal of Geophysical Research*, *114*, A01312. https://doi.org/10.1029/2008JA013643

Qian, L., Burns, A. G., Emery, B. A., Foster, B., Lu, G., Maute, A., . . . Wang, W. (2014). The NCAR TIE-GCM. In J. Huba, R. Schunk, & G. Khazanov (Eds.), *Modeling the ionosphere-thermosphere system* (pp. 73–83). Chichester, UK: John Wiley. https://doi.org/10.1002/9781118704417.ch7

Rees, M. H., & Roble, R. G. (1975). Observations and theory of the formation of stable auroral red arcs. *Reviews of Geophysics*, *13*(1), 201–242. https://doi.org/10.1029/RG013i001p00201

Richmond, A. D., Ridley, E. C., & Roble, R. G. (1992). A thermosphere/ionosphere general circulation model with coupled electrodynamics. *Geophysical Research Letters*, *19*(6), 601–604. https://doi.org/10.1029/92GL00401

Ronksley, A. (2016). Optical remote sensing of mesoscale thermospheric dynamics above Svalbard and Kiruna (PhD Thesis). UK: University College London.

Sandholt, P. E., Farrugia, C. J., Moen, J., Noraberg, Ø., Lybekk, B., Sten, T., & Hansen, T. (1998). A classification of dayside auroral forms and activities as a function of interplanetary magnetic field orientation. *Journal of Geophysical Research*, *103*(A10), 23,325–23,345. https://doi.org/10.1029/98JA02156

Schlegel, K., Lühr, H., St-Maurice, J.-P., Crowley, G., & Hackert, C. (2005). Thermospheric density structures over the polar regions observed with CHAMP. *Annales Geophysicae*, *23*(5), 1659–1672. https: //doi.org/10.5194/angeo-23-1659-2005

Schunk, R. W., & Nagy, A. F. (1978). Electron temperatures in the F region of the ionosphere: Theory and observations. *Reviews of Geophysics*, *16*(3), 355–399. https://doi.org/10.1029/RG016i003p00355

Shepherd, G. G. (1979). Dayside cleft aurora and its ionospheric effects. *Reviews of Geophysics*, *17*(8), 2017–2033. https://doi.org/10.1029/RG017i008p02017

Sims, G., Ashley, M. C. B., Cui, X., Everett, J. R., Feng, L., Gong, X., . . . Zhu, Z. (2012). Airglow and aurorae at dome A, Antarctica. *Publications of the Astronomical Society of the Pacific*, *124*(916), 637–649.

Sojka, J., Schunk, R., David, M., Innis, J., Greet, P., & Dyson, P. (2001). A theoretical model study of F-region response to high latitude neutral wind upwelling events. *Journal of Atmospheric and Solar-Terrestrial Physics*, *63*(14), 1571–1584. https://doi.org/10.1016/S1364-6826(01)00035-9

Solomon, S. C., Hays, P. B., & Abreu, V. J. (1988). The auroral 6300 Å emission: Observations and modeling. *Journal of Geophysical Research*, *93*(A9), 9867–9882. https://doi.org/10.1029/JA093iA09p09867

Su, F., Wang, W., Burns, A. G., Yue, X., & Zhu, F. (2015). The correlation between electron temperature and density in the topside ionosphere during 2006–2009. *Journal of Geophysical Research: Space Physics*, *120*, 10,724–10,739. https://doi.org/10.1002/2015JA021303

Thomas, L. D., & Nesbet, R. K. (1975). Low-energy electron scattering by atomic oxygen. *Physical Review A*, *11*, 170–173. https://doi.org/10.1103/PhysRevA.11.170

Trattner, K. J., Mulcock, J. S., Petrinec, S. M., & Fuselier, S. A. (2007). Probing the boundary between antiparallel and component reconnection during southward interplanetary magnetic field conditions. *Journal of Geophysical Research*, *112*, A08210. https://doi.org/10.1029/2007JA012270

Vontrat-Reberac, A., Fontaine, D., Blelly, P.-L., & Galand, M. (2001). Theoretical predictions of the effect of cusp and dayside precipitation on the polar ionosphere. *Journal of Geophysical Research*, *106*(A12), 28,857–28,865. https://doi.org/10.1029/2001JA900131

Wickwar, V. B., & Kofman, W. (1984). Dayside red auroras at very high latitudes: The importance of thermal excitation. *Geophysical Research Letters*, *11*(9), 923–926. https://doi.org/10.1029/GL011i009p00923

Zhou, X. W., Russell, C. T., Le, G., Fuselier, S. A., & Scudder, J. D. (2000). Solar wind control of the polar cusp at high altitude. *Journal of Geophysical Research*, *105*(A1), 245–251. https://doi.org/10.1029/1999JA900412